



Accuracy Analysis of Finite-Difference Methods on Non-Uniform Grids

Andreas Babucke, Markus J. Kloker

IB 09-01

With increasing computational power, highly accurate direct numerical simulations of unsteady shear-flow phenomena in large domains or complex geometries are feasible nowadays. These new possibilities require non-uniform grids, either for more efficient computing or a specific geometry not covered by an equidistant mesh. We revisit this issue with a rigorous spectral analysis which has been approved on equidistant grids. Two transformation techniques and directly applied biased finite differences are compared theoretically and numerically for the one-dimensional linear advection-diffusion problem, considering explicit and compact finite differences of 2^{nd} and 4^{th} order. In the numerical experiment with sudden grid coarsening and refinement, both biased finite differences and transformation with numerically computed metric coefficients give similar results. Despite one might expect analytical metric coefficients to be the best choice, this numerical example reveals its poor accuracy compared to the other two implementations. Finally, the evolution of a Tollmien-Schlichting wave in a compressible boundary-layer flow has been simulated on a streamwise non-equidistant grid and compared with linear stability theory and a direct numerical simulation on an equidistant grid.

1 Introduction

The first direct numerical simulations (DNS) of laminar instability or laminar-to-turbulent transition of boundary-layer flows were based on equidistant cartesian grids computing

1 Introduction

unsteady flows along rather simple geometries like a flat plate, see e.g. [7, 10]. Nowadays increased computational power allows a wider range of applications for DNS. It is obvious that complex geometries require a non-uniform mesh, as used in [1, 12, 13] for example. But also for simple geometries it may be necessary to use non-equidistant grids. For direct aeroacoustic computations [3, 6], the flow as well as the relevant portions of the acoustic farfield have to be computed, leading to huge domains. Here, grid stretching is necessary to use the computational resources efficiently. A second requirement for aeroacoustic simulations is the construction of sponge regions for the outflow boundary. They are the crucial part for spatial simulations of transition and aeroacoustic simulations as high-amplitude disturbances have to be prevented reaching the outflow in order not to spoil the low-amplitude disturbance/acoustic field with reflections. Colonius et al. [5] use a combination of grid stretching and spatial low-pass filtering to dissipate downstream propagating disturbances in the sponge zone of the aeroacoustic simulation. Visbal and Gaitonde [15] have shown the practical application of finite differences on deformed meshes using grid transformation. They found high-order schemes to be superior to low-order discretization. The effect of skewed meshes on the stability and accuracy of finite differences (FD) has been studied by You et al. [16]: they found large numerical dissipation on skewed grids which may negatively affect the stability of the computation. A special implementation of curved-linear meshes is proposed by Zhong and Tatieni [17]: the actual stretching is included in the coefficients of the stencil and grid transformation is used only for the bending of the mesh.

On equidistant grids, dispersion and dissipation properties have been evaluated by the real and imaginary part of the modified wave number by Lele [11]. The combination of spatial discretization and time-advancing scheme has been considered by Kloker [10]. As such an analysis is based on an infinite or periodic domain, it is not directly applicable to non-uniform grids, especially for compact schemes.

Based on a one-dimensional linear convection-diffusion problem three principal possibilities for a finite difference (FD) discretization on non-uniform grids are compared. The first way is to use a biased stencil according to the coordinates of the grid, see e.g. [14]. The other two implementations are based on a transformation of the physical non-uniform grid to a computational equidistant grid with either analytically or numerically computed metric coefficients. Explicit FDs are investigated theoretically in section 2 considering the modified wave number. Since this analysis is hardly feasible for compact schemes, numerical examination based on the one-dimensional advection-diffusion equation is performed in section 3. In section 4 the DNS of the spatial evolution of a Tollmien-Schlichting wave over an almost instantaneous coarsening of the mesh is simulated. Finally, the main results are summarized in section 5.

2 Modified-Wavenumber Analysis

The principles of different implementations of non-uniform grids are investigated by solving the one-dimensional linear advection-diffusion equation

$$\frac{\partial u}{\partial t} + c \cdot \frac{\partial u}{\partial x} = d \cdot \frac{\partial^2 u}{\partial x^2} \quad , \quad c, d \in \mathbb{R} \wedge \geq 0 \quad (1)$$

on a periodic or infinite domain in x-direction with constant diffusion and convection speed. The evaluation of the spatial discretization is based on a wave with the wavenumber k , allowing an arbitrary phase Θ :

$$u(x) = \Re(e^{i(k \cdot x + \Theta)}) = \cos(k \cdot x + \Theta). \quad (2)$$

For the computation of spatial derivatives on a non-uniform grid, the biased scheme uses the coordinates of the neighboring grid points to compute the stencil for the corresponding finite difference. This has to be done once after the grid has been defined. If grid transformation is applied, spatial derivatives in physical space are computed by finite differences on an equidistant computational grid and multiplying them with the corresponding metric coefficients. For the one-dimensional case, the transformation for the first and second derivatives simplifies to

$$\frac{\partial}{\partial x} = \frac{1}{\left(\frac{\partial x}{\partial \xi}\right)} \cdot \frac{\partial}{\partial \xi} \quad (3)$$

$$\frac{\partial^2}{\partial x^2} = \frac{1}{\left(\frac{\partial x}{\partial \xi}\right)^2} \cdot \frac{\partial^2}{\partial \xi^2} - \frac{\frac{\partial^2 x}{\partial \xi^2}}{\left(\frac{\partial x}{\partial \xi}\right)^3} \cdot \frac{\partial}{\partial \xi}, \quad (4)$$

with the metric coefficients $\partial x / \partial \xi$ and $\partial^2 x / \partial \xi^2$ defined by the transformation $x = x(\xi)$. Being derivatives in computational space, the metric coefficients can be computed either numerically using the same procedure as for the flow variables or analytically if the transformation $x(\xi)$ is given analytically.

2.1 Finite differences on equidistant grids

The classical analysis of finite differences for solutions of equation (2) on equidistant grids is based on the modified wavenumber k_{mod}^* , which is the normalized first derivative and k_{mod}^{*2} , which is the normalized second derivative, respectively [10, 11]:

$$k_{mod}^* = -i \cdot \Delta x \cdot \frac{(\partial u / \partial x)_{mod}}{u}, \quad k_{mod}^{*2} = -\Delta x^2 \cdot \frac{(\partial^2 u / \partial x^2)_{mod}}{u}, \quad (5)$$

2 Modified-Wavenumber Analysis

with $i = \sqrt{-1}$ and $k_{mod}^* = k_{mod}\Delta x$. The real part of the modified wavenumber k_{mod}^* describes the dispersion relation which is shown in figure 1 for various central explicit and compact finite differences. Higher-order as well as compact schemes provide better wave representation even for less resolved waves. For non-central schemes, also imaginary parts of k_{mod}^* exist. This corresponds to a phase shift of the computed derivative, resulting in damping or amplification, depending on the direction of the advection speed. From the maximum of k_{mod}^* onwards, aliasing occurs since the group velocity is proportional to $\partial k_{mod}^*/\partial k^*$. For the second derivative, the analysis is based on the modified wavenumber square k_{mod}^{*2} , with its real part representing the damping given by the diffusion equation (1). To compute the second derivative, one might either apply the first derivative twice or evaluate it directly with the coefficients of a second-derivative FD. A comparison of these methods is illustrated in figure 2 for an explicit and a compact scheme of 4th and 6th order, respectively. The direct evaluation of the second derivatives yields much better results: i) a better accordance with the exact solution k^{*2} and ii) a non-vanishing k_{mod}^{*2} for the least-resolved wave ($k^* = \pi$). The finite value of the second derivative for the saw-tooth mode provides a markedly more stable and consistent numerical scheme, especially for non-linear computations as high-wavenumber waves are damped by viscous terms. If non-central finite differences are used, the phase shift of the second derivative causes an artificial advection, given by the imaginary part of k_{mod}^{*2} .

2.2 Explicit finite differences on non-uniform grids

To evaluate the properties of finite differences on a non-uniform physical grid, the biased stencils or the metric coefficients need to be taken into account. Therefore, a specific grid stretching has to be defined with the analysis being only valid for this type of mesh. To achieve generally valid results, a generic function $x(\xi)$ is desirable. In contrast to the uniform grid, an analytical approach providing wavenumber diagrams as in figures 1 and 2 is now only possible for *explicit* finite differences. Due to the varying resolution, the quality of the computed derivative differs at the neighboring points. An analytical expression of the modified wavenumber is no more possible without specifying the mesh on the whole computational domain. Thus, the properties of *compact* finite differences have to be investigated using a numerical experiment, as done in section 3.2.

The probably most generic grid transformation is a continuous increase or decrease of the grid spacing Δx in physical space which can be expressed by an exponential function:

$$x(\xi) = e^{c \cdot \xi}, \quad \frac{\partial x}{\partial \xi} = c \cdot x, \quad \frac{\partial^2 x}{\partial \xi^2} = c^2 \cdot x, \quad (6)$$

2 Modified-Wavenumber Analysis

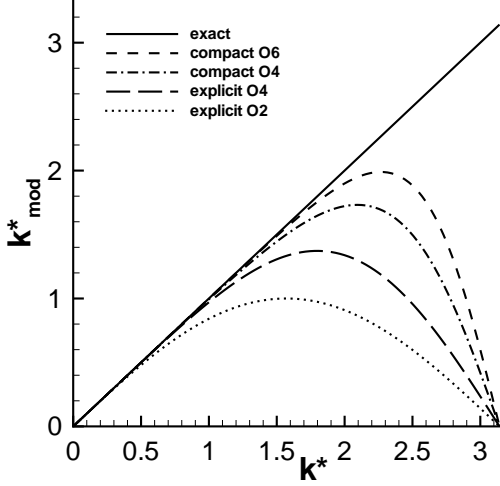


Figure 1: Modified wavenumber k_{mod}^* for central explicit and compact schemes up to 6th order.

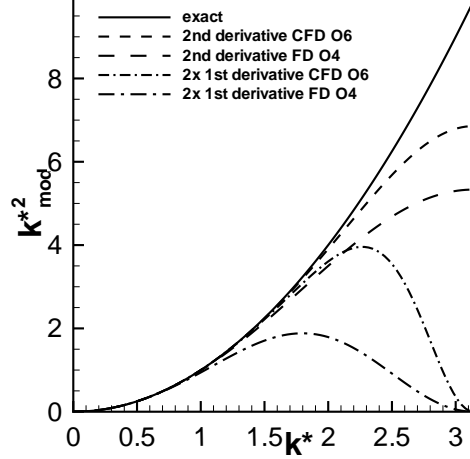


Figure 2: Modified wavenumber square k_{mod}^{*2} for direct calculation of the second derivative versus applying the first derivative twice (4th and 6th order).

where c determines the strength of the continuous stretching. Multiplication with the step size in computational space, $\Delta\xi$, gives the non-dimensional parameter $c^* = c \cdot \Delta\xi$. With the analytical grid stretching we can define a reference step size in physical space

$$\Delta x_{ref} = \left. \frac{\partial x}{\partial \xi} \right|_{an.} \cdot \Delta \xi = c^* \cdot x \quad (7)$$

that is used to obtain the non-dimensional wavenumber $k^* = k \cdot \Delta x_{ref}$. Note that half the grid spacings of a “centered” stencil are smaller or larger than Δx_{ref} , respectively. With the coordinates based on equation (7), we obtain the values of the considered wave with an arbitrary phase Θ :

$$\begin{aligned} u_{j-2} &= e^{i\left(\frac{k^*}{c^*} \cdot e^{-2 \cdot c^*} + \Theta\right)}, & u_{j-1} &= e^{i\left(\frac{k^*}{c^*} \cdot e^{-c^*} + \Theta\right)}, & u_j &= e^{i\left(\frac{k^*}{c^*} + \Theta\right)}, \\ u_{j+1} &= e^{i\left(\frac{k^*}{c^*} \cdot e^{c^*} + \Theta\right)}, & u_{j+2} &= e^{i\left(\frac{k^*}{c^*} \cdot e^{2 \cdot c^*} + \Theta\right)}. \end{aligned} \quad (8)$$

For biased finite differences, the spatial derivatives are computed directly in physical space

$$\frac{\partial u}{\partial x} \simeq \mathbf{a} \cdot u_{j-2} + \mathbf{b} \cdot u_{j-1} + \mathbf{c} \cdot u_j + \mathbf{d} \cdot u_{j+1} + \mathbf{e} \cdot u_{j+2} \quad (9)$$

2 Modified-Wavenumber Analysis

with the coordinates being included in the coefficients. Their derivation is based on a Taylor-series expansion at the considered point x_j . The coefficients for the first and second derivatives are listed in tables 1 and 2.

In case of grid transformation, the grid is considered in terms of metric coefficients and not by the stencil of the finite difference itself. For the evaluation of metric coefficients and spatial derivatives in computational ξ -space, standard finite differences are used. The resulting metric terms are provided by equations (10)-(11) and (12)-(13) for analytical and numerical grid transformation, respectively:

$$\frac{\partial x}{\partial \xi_{an.}} = c \cdot x = \frac{\Delta x_{ref}}{\Delta \xi} \quad (10)$$

$$\frac{\partial^2 x}{\partial \xi^2_{an.}} = c^2 \cdot x = c^* \frac{\Delta x_{ref}}{\Delta \xi^2} \quad (11)$$

$$\frac{\partial x}{\partial \xi_{num.}} = \Delta x_{ref} (\mathbf{a} \cdot e^{-2c^*} + \mathbf{b} \cdot e^{-c^*} + \mathbf{c} + \mathbf{d} \cdot e^{c^*} + \mathbf{e} \cdot e^{2c^*}) \quad (12)$$

$$\frac{\partial^2 x}{\partial \xi^2_{num.}} = \Delta x_{ref} (\mathbf{a} \cdot e^{-2c^*} + \mathbf{b} \cdot e^{-c^*} + \mathbf{c} + \mathbf{d} \cdot e^{c^*} + \mathbf{e} \cdot e^{2c^*}) . \quad (13)$$

With the derivatives in physical space, the modified wavenumber and its square can be easily computed from equation (5). For two exemplary grid-stretching factors, the real and imaginary parts of the modified wavenumber k_{mod}^* and the wave number square k_{mod}^{*2} are shown for the first and second derivative, respectively. The chosen values of $c^* = 1$ and $c^* = 0.3$ correspond to an increase of the physical step size Δx by a factor of $e = 2.718$ and 1.35 , respectively. Thus the resolution of a wave at the outer left and right grid points of a five-point stencil differs by a factor of 20 for $c^* = 1$. Despite one would not choose such a strong stretching for real applications, it clearly demonstrates the properties of the three different discretization methods on non-uniform grids.

The real and imaginary parts of the modified wavenumber k_{mod}^* of the first derivative based on three- and five-point stencils are shown in figures 3 and 4, respectively. The range of normalized wavenumber $0 \leq k^* \leq \pi$ in the plots is somewhat arbitrary. With the wavenumber k being normalized with Δx_{ref} , the value $k^* = \pi$ does not correspond to least resolved wave as it is known from equidistant grids. Using the locally varying gridsize Δx , the resolution may be expressed in terms of points per wavelength λ_x :

$$\frac{n_{points}}{\lambda_x} = \frac{2\pi}{k \cdot \Delta x} = \frac{2\pi}{k^* \cdot \frac{\Delta x}{\Delta x_{ref}}} . \quad (14)$$

2 Modified-Wavenumber Analysis

$\frac{\partial}{\partial x}$	$\mathcal{O}2$	$\mathcal{O}4$
a	0	$\frac{\Delta x_{m1} \Delta x_{p1} \Delta x_{p2}}{\Delta x_{m2} (\Delta x_{p2} + \Delta x_{m2}) (\Delta x_{p1} + \Delta x_{m2}) (\Delta x_{m2} - \Delta x_{m1})}$
b	$-\frac{\Delta x_{p1}}{\Delta x_{m1} (\Delta x_{p1} + \Delta x_{m1})}$	$\frac{\Delta x_{m2} \Delta x_{p1} \Delta x_{p2}}{\Delta x_{m2} \Delta x_{p1} \Delta x_{p2}} - \frac{\Delta x_{m1} (\Delta x_{p2} + \Delta x_{m1}) (\Delta x_{p1} + \Delta x_{m1}) (\Delta x_{m2} - \Delta x_{m1})}{(\Delta x_{m1} \Delta x_{m2} \Delta x_{p1} + (\Delta x_{m1} \Delta x_{m2} \Delta x_{p2}) - (\Delta x_{m1} \Delta x_{p1} \Delta x_{p2}) - (\Delta x_{m2} \Delta x_{p1} \Delta x_{p2})}$
c	$\frac{\Delta x_{p1} - \Delta x_{m1}}{\Delta x_{p1} \Delta x_{m1}}$	$\frac{\Delta x_{m2} \Delta x_{m1} \Delta x_{p1} \Delta x_{p2}}{\Delta x_{m2} \Delta x_{m1} \Delta x_{p1} \Delta x_{p2}} - \frac{\Delta x_{p1} (\Delta x_{p1} - \Delta x_{p2}) (\Delta x_{p1} + \Delta x_{m1}) (\Delta x_{p1} + \Delta x_{m2})}{\Delta x_{m2} \Delta x_{m1} \Delta x_{p1} \Delta x_{p2}}$
d	$\frac{\Delta x_{m1}}{\Delta x_{p1} (\Delta x_{p1} + \Delta x_{m1})}$	$\frac{\Delta x_{m2} \Delta x_{m1} \Delta x_{p1}}{\Delta x_{m2} \Delta x_{m1} \Delta x_{p1}} - \frac{\Delta x_{p2} (\Delta x_{p2} + \Delta x_{m1}) (\Delta x_{p2} + \Delta x_{m2}) (\Delta x_{p1} - \Delta x_{p2})}{\Delta x_{m2} \Delta x_{m1} \Delta x_{p1} \Delta x_{p2}}$
e	0	$\frac{\Delta x_{m2} \Delta x_{m1} \Delta x_{p1}}{\Delta x_{m2} \Delta x_{m1} \Delta x_{p1}}$

Table 1: Coefficients of explicit biased finite differences for the first derivative of 2^{nd} and 4^{th} order accuracy. Step sizes are defined as $\Delta x_{m2} = (x_j - x_{j-2})$, $\Delta x_{m1} = (x_j - x_{j-1})$, $\Delta x_{p1} = (x_{j+1} - x_j)$ and $\Delta x_{p2} = (x_{j+2} - x_j)$.

$\frac{\partial^2}{\partial x^2}$	$\mathcal{O}2$	$\mathcal{O}4$
a	0	$-2 \frac{\Delta x_{p1} \Delta x_{p2} - \Delta x_{m1} \Delta x_{p2} - \Delta x_{m1} \Delta x_{p1}}{\Delta x_{m2} (\Delta x_{m2} + \Delta x_{p2}) (\Delta x_{m1} - \Delta x_{m2}) (\Delta x_{p2} + \Delta x_{m2})}$
b	$\frac{2}{\Delta x_{m1} (\Delta x_{m1} + \Delta x_{p1})}$	$2 \frac{\Delta x_{p1} \Delta x_{p2} - \Delta x_{m2} \Delta x_{p2} - \Delta x_{m2} \Delta x_{p1}}{\Delta x_{m1} (\Delta x_{m1} + \Delta x_{p1}) (\Delta x_{m1} + \Delta x_{p2}) (\Delta x_{m1} - \Delta x_{m2})}$
c	$\frac{2}{-\Delta x_{m1} \Delta x_{p1}}$	$2 \frac{(\Delta x_{p1} \Delta x_{p2}) - (\Delta x_{m1} \Delta x_{p2}) - (\Delta x_{m1} \Delta x_{p1}) - (\Delta x_{m2} \Delta x_{p1}) + (\Delta x_{m1} \Delta x_{m2})}{\Delta x_{m2} \Delta x_{m1} \Delta x_{p1} \Delta x_{p2}}$
d	$\frac{2}{\Delta x_{p1} (\Delta x_{m1} + \Delta x_{p1})}$	$2 \frac{\Delta x_{m1} \Delta x_{p2} + \Delta x_{m2} \Delta x_{p2} - \Delta x_{m1} \Delta x_{m2}}{\Delta x_{m2} (\Delta x_{m2} + \Delta x_{p2}) (\Delta x_{m2} + \Delta x_{p1}) (\Delta x_{p2} - \Delta x_{p2})}$
e	0	$-2 \frac{\Delta x_{p2} (\Delta x_{m2} + \Delta x_{p2}) (\Delta x_{p2} - \Delta x_{p1}) (\Delta x_{p2} + \Delta x_{m1})}{\Delta x_{p2} (\Delta x_{m2} + \Delta x_{p2}) (\Delta x_{p2} - \Delta x_{p1}) (\Delta x_{p2} + \Delta x_{m1})}$

Table 2: Coefficients of explicit biased finite differences for the second derivative of 2^{nd} and 4^{th} order accuracy.

2 Modified-Wavenumber Analysis

The value of $k^* = \pi$ being the abscissa's maximum value in the diagrams 3 and 4 corresponds to a number of points per wavelength of 8.6, 3.2, 1.2 and 0.4 for the physical stepsizes $(x_{j-1} - x_{j-2})$, $(x_j - x_{j-1})$, $(x_{j+1} - x_j)$ and $(x_{j+2} - x_{j+1})$, respectively. For smaller values of c^* , the variation decreases. Independently of c^* , $\frac{n_{points}}{\lambda_x}$ for $k^* = \pi$ is larger than two for the first two points and smaller than two for the two right points of the stencil.

Equation 3 reveals that the first derivatives in physical space based on analytical and numerical metric coefficients simply differ by the factor of the differently computed metric terms $\frac{\partial x / \partial \xi_{num.}}{\partial x / \partial \xi_{an.}}$. Thus the real and imaginary parts of the modified wavenumbers for analytical and numerical computed metric terms vary only by this factor.

2.2.1 First Derivative based on 3-Point Stencil

As one can see in figure 3 a), the biased finite difference provides the best dispersion properties for the three-point stencil on the exponentially stretched grid with $c^* = 1$. Compared to analytically and numerically computed metric coefficients, the characteristic of the biased discretization differs less from the exact solution $k_{mod,r,exact}^* = k^*$. The analytical metric coefficients result in higher values for both real and imaginary parts of the modified wave number than the numerically computed metrics. In case of analytical metric coefficients, the increase $\partial k_{mod,r}^* / \partial k^*$ of the modified wavenumber is slightly too large for well resolved waves. For numerically computed metric coefficients, good wave propagation properties are achieved up to $k^* \approx 0.6$. Aliasing occurs for both grid-transformation methods for values $k^* > 1$. If a biased FD is used, the imaginary part $k_{mod,i}^*$ of the modified wave number becomes negative (figure 3 b). Thus, waves traveling in the direction of grid coarsening are successively damped. For the methods involving metric terms, these waves are amplified with increasing wave number up to $k^* \approx 2.7$. Less resolved waves ($k^* > 2.7$) are slightly damped.

For the weaker stretching $c^* = 0.3$, real and imaginary parts of the modified wave number are given in figures 3 c) and d), respectively. Now, all three methods provide similar results for the real part $k_{mod,r}^*$ with the dispersion relation being almost equal to 2nd-order FDs on a uniform mesh (see figure 1). The limiting factor for the accuracy is the imaginary part $k_{mod,i}^*$. In case of grid transformation, notable amplification for waves in the direction of grid coarsening exists. Also for smaller stretching ratios, this can not be neglected: e.g. a stepsize increase of 10% ($c^* = 0.1$) yields a maximum of $k_{mod,i}^* = 0.09$.

2 Modified-Wavenumber Analysis

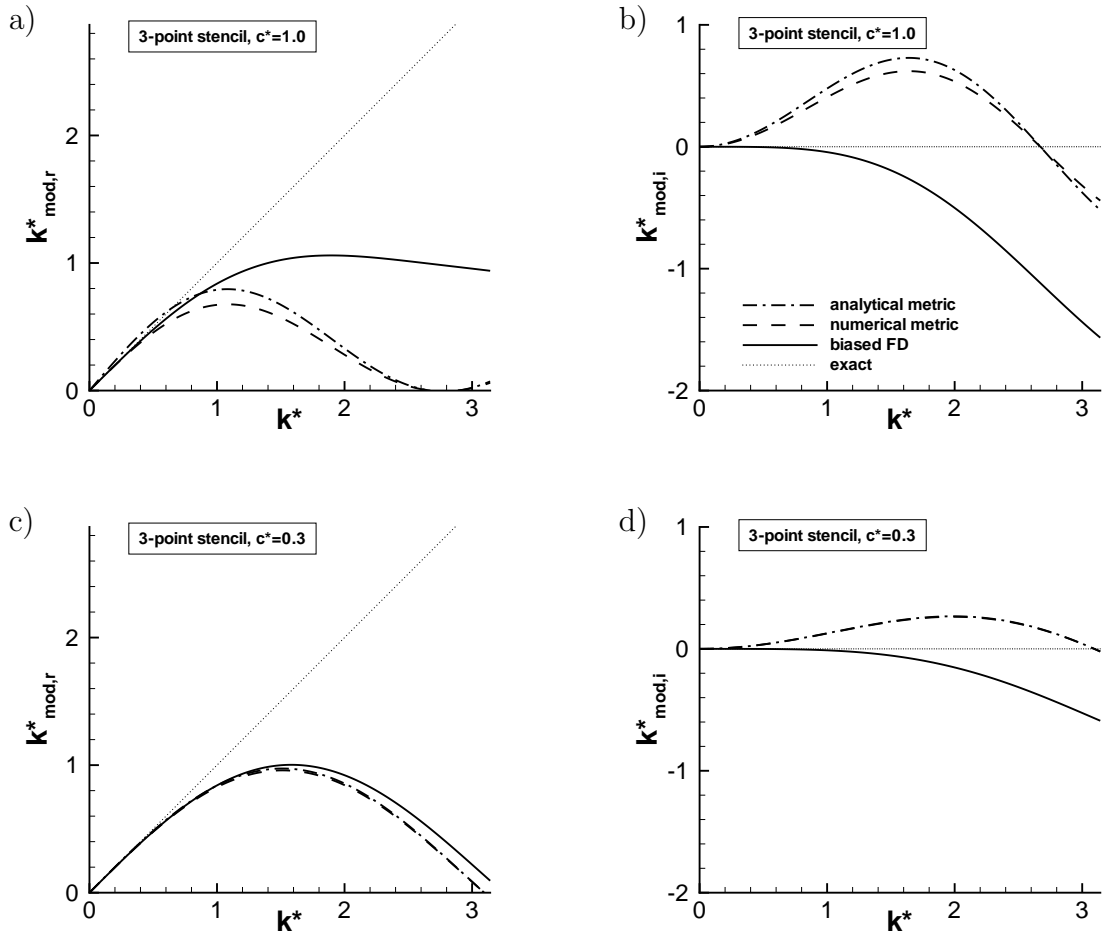


Figure 3: Real and imaginary parts of the modified wave number k_{mod}^* for stretching factors $c^* = 1.0$ and $c^* = 0.3$ using explicit finite differences based on 3-point stencils.

2.2.2 First Derivative based on 5-Point Stencil

For the larger stencils, again the biased FD gives the best results in terms of wave propagation, as shown in figure 4 a) for $c^* = 1$. The difference between analytically and numerically evaluated metrics is less obvious than for the discretization based on second order FDs. The absolute values of the real and imaginary parts are slightly larger for the numerical grid transformation. Now, acceptable wave propagation properties are possible only up to $k^* \approx 0.3$. This smaller value compared to the three-point stencil is due to the fact that a stronger grid stretching is included in the stencil with the outer point x_{j+2} of the FD. Like for the three-point stencil, poorly resolved waves are damped for the 4th-order biased discretization as they propagate in the direction of coarsening since $k_{mod,i,bias}^* < 0$. This is also the case for grid-transformation methods in the range of $0.4 < k^* < 2.7$. Waves with smaller wave numbers are only slightly amplified compared to the least resolved waves exhibiting a distinct amplification.

The case of a weaker stretching ($c^* = 0.3$) is shown in figures 4 c) and d). Now, the 5-point stencil provides a better result than the 3-point stencil in contrast to $c^* = 1$. The value $c^* \approx 0.4$ (50% increase of step size) was found to be the limit for the 5-point stencil to be more accurate than the 3-point stencil. Compared with figure 1 a), the dispersion properties for $c^* = 0.3$ are already quite similar to the equidistant spacing. With $k_{mod,i,min}^* = -0.52$ for biased FDs and $k_{mod,i,min}^* = -0.19$ for both grid-transformation methods, dissipation is still a relevant issue. Thus, damping is only weakly affected by coarsening of the grid. An acceptably low damping ($|k_{mod,i}^*| < 0.1$) for relatively well-resolved waves ($k^* < \pi/2$) is observed for $c^* \approx 0.1$ (step size increase by 10%).

2.2.3 Order of First Derivatives

The order of a scheme describes how the leading discretization error is reduced with increased resolution. The relative error of the first derivative can be expressed by the modified wave number to

$$\epsilon = \left| \frac{\sqrt{(k_{mod,r}^*)^2 + (k_{mod,i}^*)^2} - k^*}{k^*} \right|. \quad (15)$$

Its dependence from the resolution, expressed by the number of grid points per wavelength ($= 2\pi/k^*$), is shown in figure 5 a) for the 3-point stencil with $c^* = 0.3$. Increasing the resolution by a factor of four reduces the error to one fourth in case of biased FDs and numerical metric coefficients.

2 Modified-Wavenumber Analysis

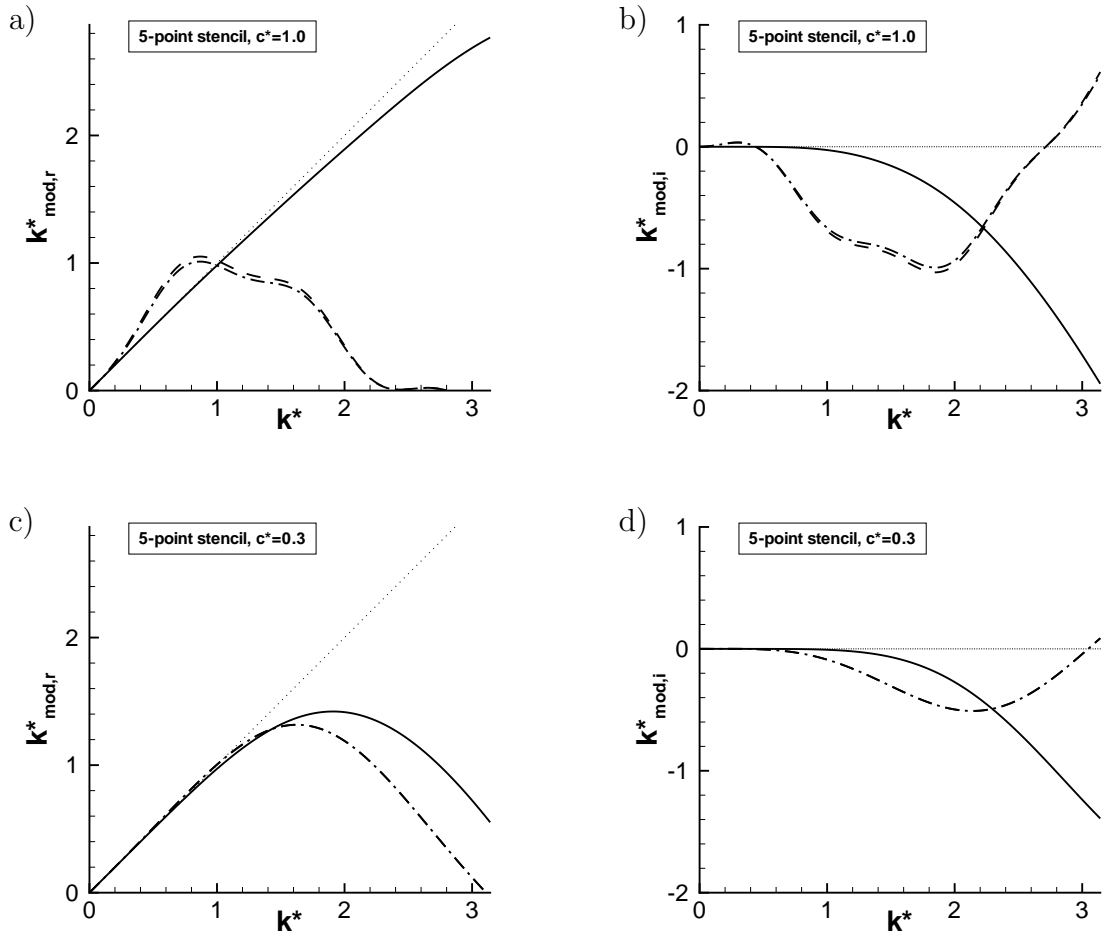


Figure 4: Real and imaginary parts of the modified wave number k_{mod}^* for stretching factors $c^* = 1.0$ and $c^* = 0.3$ using explicit finite differences based on 5-point stencils.

2 Modified-Wavenumber Analysis

Thus, these methods are of second order as it is the case on equidistant grids. With its error being limited to $\epsilon = 0.015$, the method of analytically computed metric coefficients is of zeroth order.

Figure 5 b) shows the corresponding results for the five-point stencil. Again, the biased FDs are of the same order ($\mathcal{O}4$) as on uniform grids. In case of numerically computed metrics, the error decays like for the 3-point FD. Thus, a larger stencil does not increase the order, rather the magnitude of the error is decreased. The error of analytical metric terms is bound to $\epsilon = 2 \cdot 10^{-4}$. Despite the error is reduced, it is still of $\mathcal{O}0$.

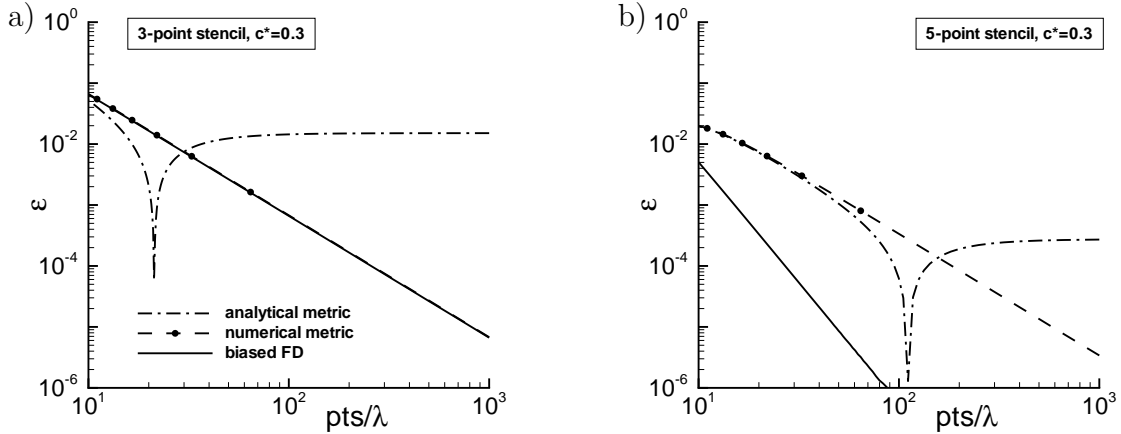


Figure 5: Relative error of the first derivative versus the resolution for stretching factor $c^* = 0.3$): a) 3-point stencil, b) 5-point stencil.

The kink in the error for analytically computed metrics occurs where errors of the real and imaginary part cancel each other. Hence, considering only the order of a scheme provides less information compared to the modified wave number analysis. In general, the order is defined as

$$\mathcal{O} = -\frac{\partial \{\log(\epsilon)\}}{\partial \{\log(pts/\lambda)\}}. \quad (16)$$

Its dependence from the stretching factor is shown in figure 6 for the 5-point stencil and $k^* = 0.311$ ($20pts/\lambda$). For vanishing grid stretching ($c^* \rightarrow 0$), numerical metric coefficients result in the fourth order known from the uniform mesh. At $c^* = 0.06$, a pole exists where amplitude and phase errors cancel each other. Then the scheme decreases to second order.

2 Modified-Wavenumber Analysis

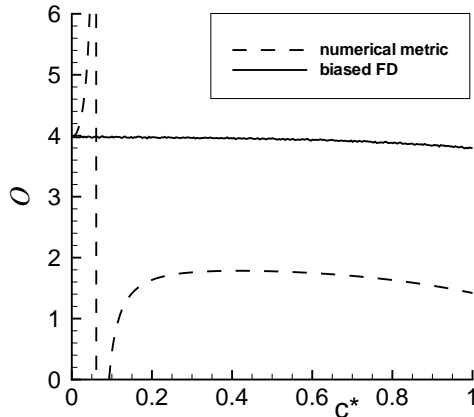


Figure 6: Discretization order \mathcal{O} of the first derivative's 5-point stencil as a function of the stretching factor c^* ($20pts/\lambda$).

It is quite astonishing that the numerical metric coefficient provides a better result. Obviously, discretization errors of the derivative in computational space and of the metric coefficients cancel each other. A remarkable fact is also that an increased stencil does not increase the order on the non-uniform grid to more than two. However, the leading error is only in the imaginary part for numerically computed metrics, resulting in an exact group velocity of up to second spectral order.

2.2.4 Second Derivative based on 3-Point Stencil

The computation of the second derivative with a second-order biased FD gives the best accordance with the exact solution k^{*2} for the real part of the modified wave number square, given in figure 7 a) for $c^* = 1$. Using numerical metric coefficients gives a similar result. However, deviation from the exact solution occurs for smaller values of k^* , and the maximum value of k_{mod}^{*2} is roughly 20% smaller than for the biased finite difference. The imaginary part is slightly smaller, thus less artificial convection is generated than is done by the biased FD. In the case of analytically computed metrics, the characteristics of k_{mod}^{*2} differs from the exact solution for the real and imaginary parts already for very small values of k^* . All three methods cause a positive value of $k_{mod,i}^{*2}$ (figure 7 b) and thus an artificial advection in the direction of grid coarsening.

For the weaker stretching $c^* = 0.3$, the real parts $k_{mod,r}^{*2}$ collapse for the three methods

2 Modified-Wavenumber Analysis

as shown in figure 7 c). Similar to the stronger stretching, a positive value of $k_{mod,i}^{*2}$ is obtained for all methods (figure 7 d). Biased FDs and numerical metric provide almost the same results, here. The value $c^* = 0.3$ is approximately the limit of acceptable accuracy for appropriately resolved waves ($k^* < \pi/2$) if biased FDs or numerically computed metric coefficients are used. Analytical metrics are an exception here, since notable values of $k_{mod,i}^{*2}$ exist even for low stretching ratios and small values of k^* .

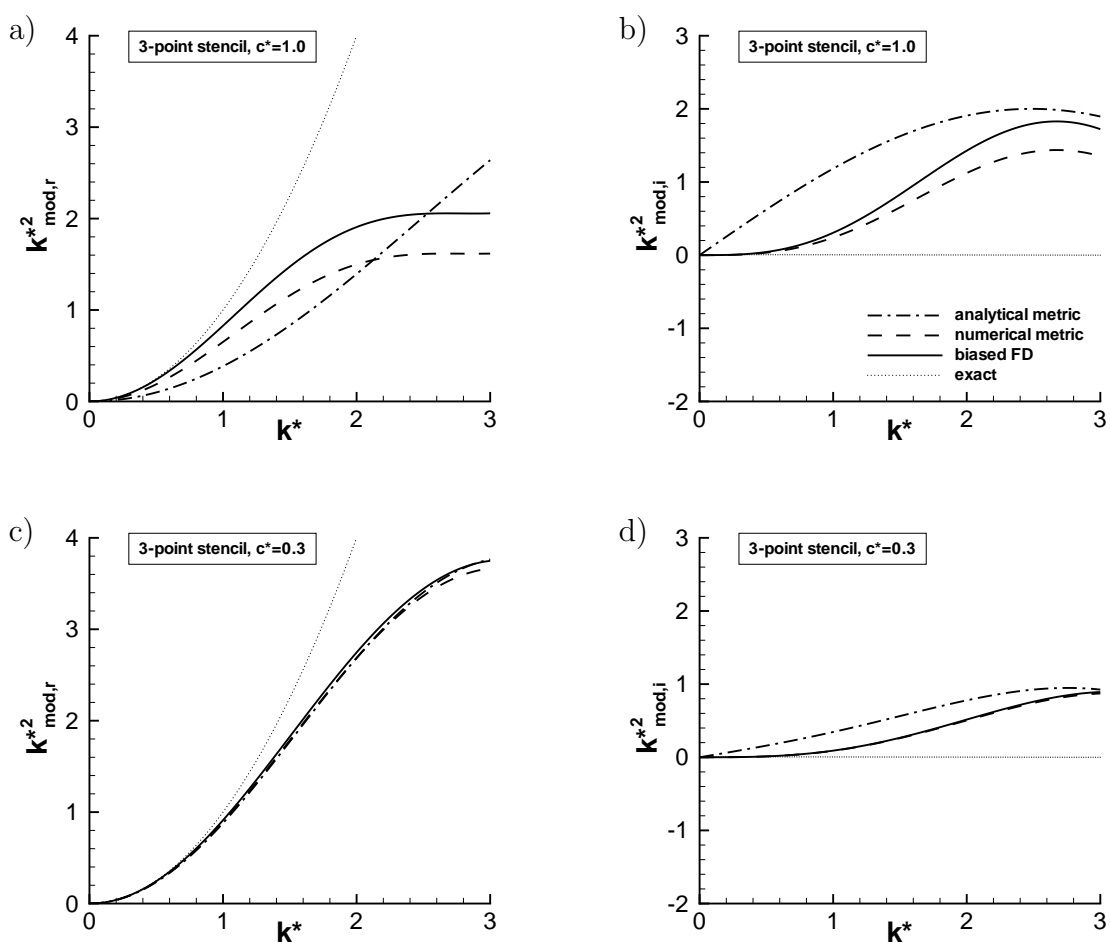


Figure 7: Real and imaginary parts of the modified wave number square k_{mod}^{*2} for stretching factors $c^* = 1.0$ and $c^* = 0.3$ based on 3-point stencil.

2.2.5 Second Derivative based on 5-Point Stencil

For the 5-point stencils applied to the stretching factor $c^* = 1$, the real parts of the modified wave number square show a better agreement with the exact solution than the 3-point stencil for all three methods (figure 8 a).

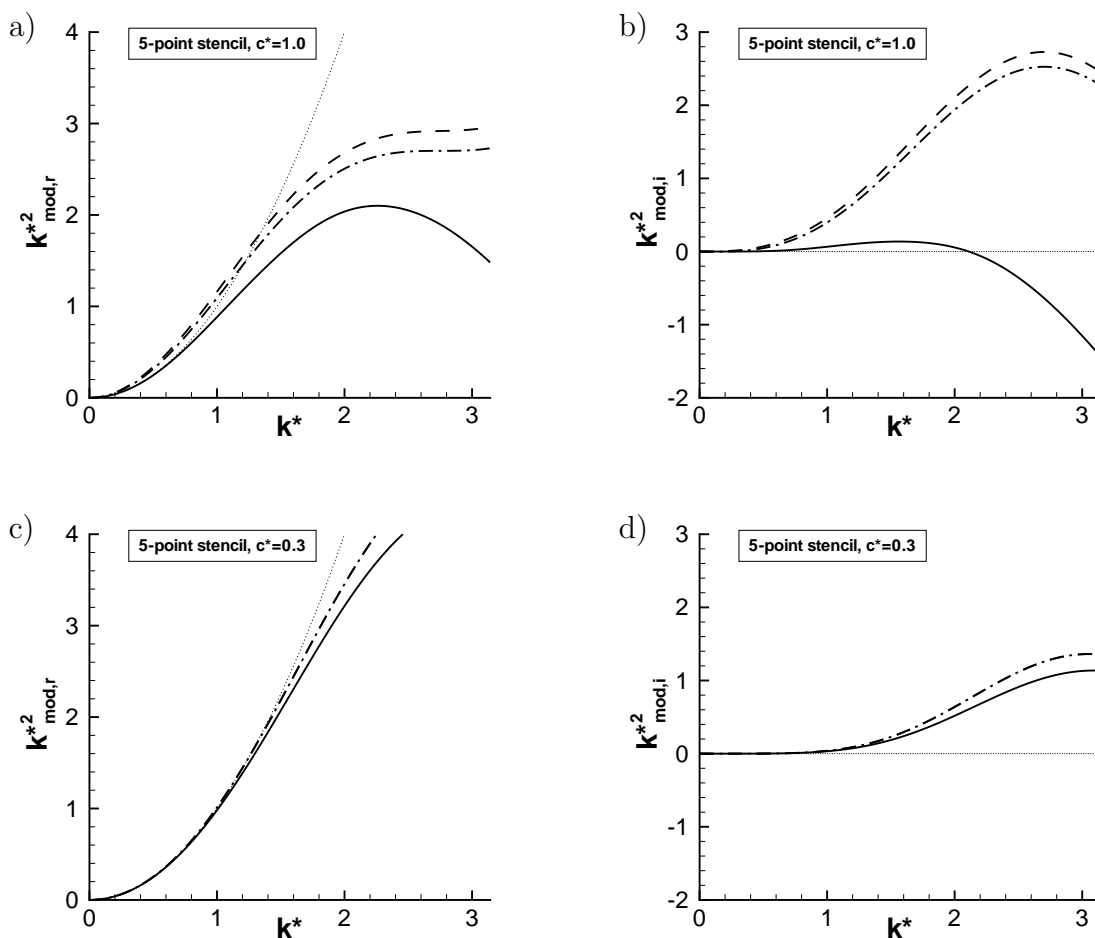


Figure 8: Real and imaginary parts of the modified wave number square k_{mod}^{*2} for stretching factors $c^* = 1.0$ and $c^* = 0.3$ based on 5-point stencil.

At small values of k^* , the weakest deviation is given for the biased finite difference. Its value grows up to $k^* = 2.25$ and decreases above. For the two methods using grid

2 Modified-Wavenumber Analysis

transformation, higher values of $k_{mod,r}^{*2}$ are reached, remaining almost constant for poorly resolved waves. The imaginary part, given in figure 8 b), differs for biased FDs and grid transformation methods. For the latter, $k_{mod,i}^{*2}$ increases up to $k^* \approx 2.8$, meaning an artificial convection in the direction of grid coarsening.

If the biased FD is used, first, the imaginary part slightly increases. For higher wave numbers, $k_{mod,i}^{*2}$ declines to negative values for $k^* > 2.1$ meaning an artificial advection in the direction of grid refinement. Unlike the first derivative, the 3-point stencil does not provide better results than the 5-point stencil when grid transformation is applied to the strong stretching ratio $c^* = 1$.

The case of weaker grid coarsening ($c^* = 0.3$) is shown in figures 8 c) and 8 d) for the real and imaginary parts of the modified wavenumber square k_{mod}^{*2} , respectively. The real part is almost the same for all three methods. Unlike for the stronger step-size ratio $c^* = 1$, biased FDs provide a positive value of $k_{mod,i}^{*2}$ similar to the grid-transformation methods. Thus, all three implementations of non-uniform grids induce an artificial advection in the direction of grid coarsening, here. Considering well-resolved waves ($k^* < \pi/2$), acceptable accuracy is achieved up to $c^* \approx 0.3$ as shown by figures 8 c) and 8 d).

2.2.6 Order of Second Derivatives

For the second derivatives, the relative error is given by

$$\epsilon = \left| \frac{\sqrt{(k_{mod,r}^{*2})^2 + (k_{mod,i}^{*2})^2} - k^{*2}}{k^{*2}} \right| \quad (17)$$

which is shown in figures 9 a) and b) for the 3- and 5-point stencils, respectively. Plotted versus the number of grid points per wave length, it allows to determine the order as done for the first derivative.

For the 3- and 5-point stencils, the biased FDs are of second and fourth order, respectively. The error of numerical metric coefficients slightly reduces reaching its final level of $\epsilon = 2 \cdot 10^{-2}$ and $\epsilon = 2 \cdot 10^{-3}$ for the 3- and 5-point stencils, respectively. Hence, the increased stencil reduces the overall error by one magnitude. For well resolved problems, the order of the second derivative computed by numerical metric coefficients is of zeroth order independently of the involved grid points. With an increasing error, the 3-point stencil provides inconsistent results. Yet this is not the case for the 5-point FD whose error behaves similar to one with the numerical metrics.

The order according to equation (16) is shown in figure 10 as a function of the stretching factor c^* for $k^* = 0.311$. On almost uniform grids ($c^* \rightarrow 0$), the order of all three

3 One-dimensional Numerical Investigation

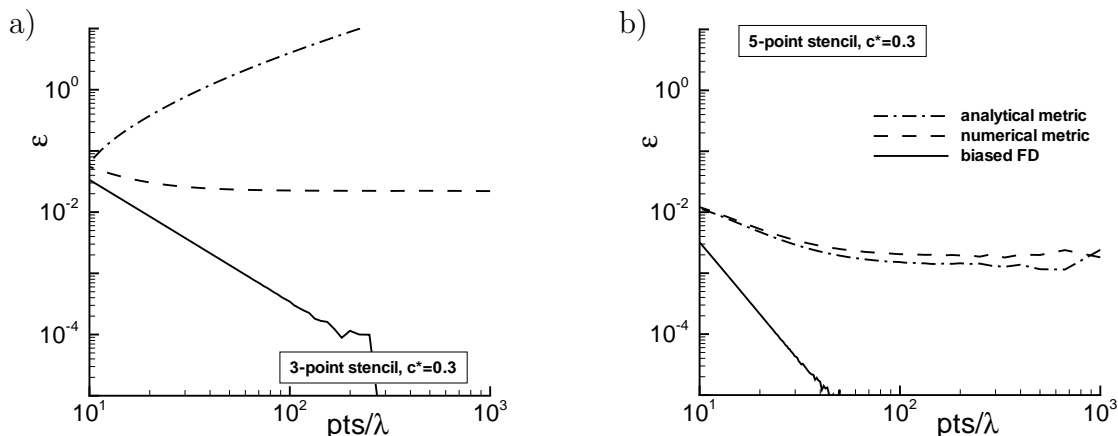


Figure 9: Relative error of the second derivative versus the resolution for stretching factor $c^* = 0.3$: a) 3-point stencil, b) 5-point stencil.

methods is consistently four. For stretching factors $c^* > 0.2$ the order of both grid transformation methods reduces linearly with c^* .

3 One-dimensional Numerical Investigation

3.1 Numerical Scheme

To investigate the effects of grid stretching for compact finite differences, we have to rely on numerical experiments. Therefore, the one-dimensional linear advection-diffusion equation (1) is solved in a periodic domain $x \in [0; x_{end}[$ with constant diffusion and advection speed. The initial condition and the resulting exact solution for this partial differential equation are given by equations (18) and (19), respectively, where $\alpha_0 = 2\pi/x_{end}$ is the fundamental wavenumber and $\alpha_k = \alpha/\alpha_0$ the number of wavelengths in the domain:

$$u_{(t=0)} = \cos(\alpha \cdot x) \quad (18)$$

$$u_{exact} = e^{-d \cdot \alpha^2 \cdot t} \cdot \cos(\alpha[x - c \cdot t]) \quad (19)$$

Time integration is done using the classical 4th-order Runge-Kutta scheme [10]. The spatial discretization is based on compact finite differences of 4th order. For the first and

3 One-dimensional Numerical Investigation

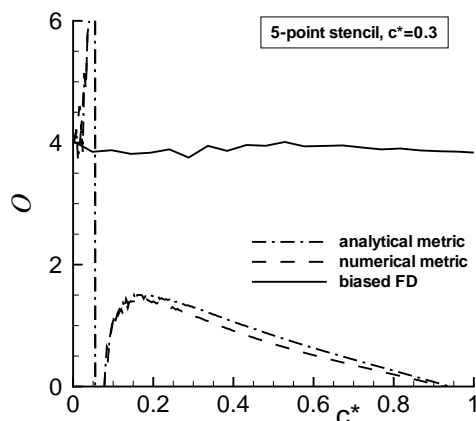


Figure 10: Discretization order \mathcal{O} of the second derivative's 5-point stencil as a function of the stretching factor c^* ($20pts/\lambda$).

second derivatives, the coefficients of the biased compact scheme are given by Shukla & Zhong [14]. For equidistant grids, the stencils for first and second derivatives reduce to

$$u'_{j-1} + 4u'_j + u'_{j+1} = \frac{3}{\Delta\xi} (u_{j+1} - u_{j-1}) \quad (20)$$

$$u''_{j-1} + 10 \cdot u''_j + u''_{j+1} = \frac{12}{\Delta\xi^2} (u_{j+1} - 2u_j + u_{j-1}) \quad , \quad (21)$$

respectively. These stencils are the standard 4th-order compact schemes with the constant step size $\Delta\xi$. The term “standard” means that the order is maximal for the stencil width. In case of grid transformation, the physical non-uniform grid is mapped on an equidistant computational grid. Spatial derivatives in physical space are then computed by equations (20) and (21) using the derivatives in computational space and multiplying them with the corresponding local metric coefficients at point x_j , given by equation (3) and (4). Additionally, explicit finite differences as discussed in section 2.2 are implemented to see the difference between explicit and compact discretization on non-uniform grids.

3.2 Results

The used grid is stretched in the first half of the domain according to the transformation given below:

$$x(\xi) = \frac{1+s}{2} \cdot \xi + \frac{s-1}{2b} \cdot [\ln(\cosh(b(\xi - \xi_1))) - \ln(\cosh(-b\xi_1))] \quad (22)$$

$$\frac{\partial x}{\partial \xi} = \frac{s-1}{b} \cdot \tanh(b(\xi - \xi_1)) + \frac{1+s}{2} \quad (23)$$

$$\frac{\partial^2 x}{\partial \xi^2} = \frac{b(s-1)}{2} - \frac{b(s-1) \sinh(b(\xi - \xi_1))^2}{\cosh(b(\xi - \xi_1))^2}. \quad (24)$$

In order to have an almost sudden coarsening of the grid given by an analytical function, the metric coefficient $\partial x/\partial \xi$ is modelled by a tanh function. The grid stretching is defined by the ratio $s = \Delta x_{max}/\Delta x_0$. The mesh starts with the regular stepsize Δx_0 , increasing to the coarse Δx_{max} at the position ξ_1 . The parameter b defines how fast the stepsize is increased: large values of b compress the tanh profile of $\partial x/\partial \xi$ leading to a sharp switch from fine to coarse spacing. The following refinement of the grid is done accordingly.

For the current investigation a computational grid with 100 points and a regular spacing of $\Delta x_0 = \Delta \xi = 0.03141$ has been used. In half the domain, the spacing is $\Delta x = 4 \cdot \Delta x_0$ with $s = 4$. The stretched area is located in the middle of the domain with $\xi_1 = 1/4\xi_{end}$ ($x_1 = 0.8$) and $\xi_2 = 3/4\xi_{end}$ ($x_2 = 7.0$) being the begin of coarsening and refinement, respectively. With $b = 100$, a rapid transition between the different stepsizes is achieved. The total length of the domain is 7.8525, resulting in a fundamental wavenumber $\alpha_0 = 0.8$ of the domain. Figure 11 shows the grid transformation $x(\xi)$ and the metric coefficients $x_\xi = \partial x/\partial \xi$ and $x_{\xi\xi} = \partial^2 x/\partial \xi^2$ for analytical and numerical evaluation.

The effect of different grid-stretching mechanisms is investigated by computing (i) a pure convection case ($c = 1, d = 0$) and (ii) a pure diffusion problem ($c = 0, d = 1$). The initial condition of both cases contains $n_\alpha = \alpha/\alpha_0 = 4$ wavelengths inside the domain. With the non-dimensional wave numbers $k^* = \alpha \cdot \Delta x = 0.025$ and $k^* = \alpha \cdot s\Delta x = 0.1$, the wave is well resolved with 250 and 62.5 points per wavelength in the fine and coarse regions, respectively. Therefore, the change of the grid and not the actual resolution mainly effects the accuracy of the result here.

3 One-dimensional Numerical Investigation

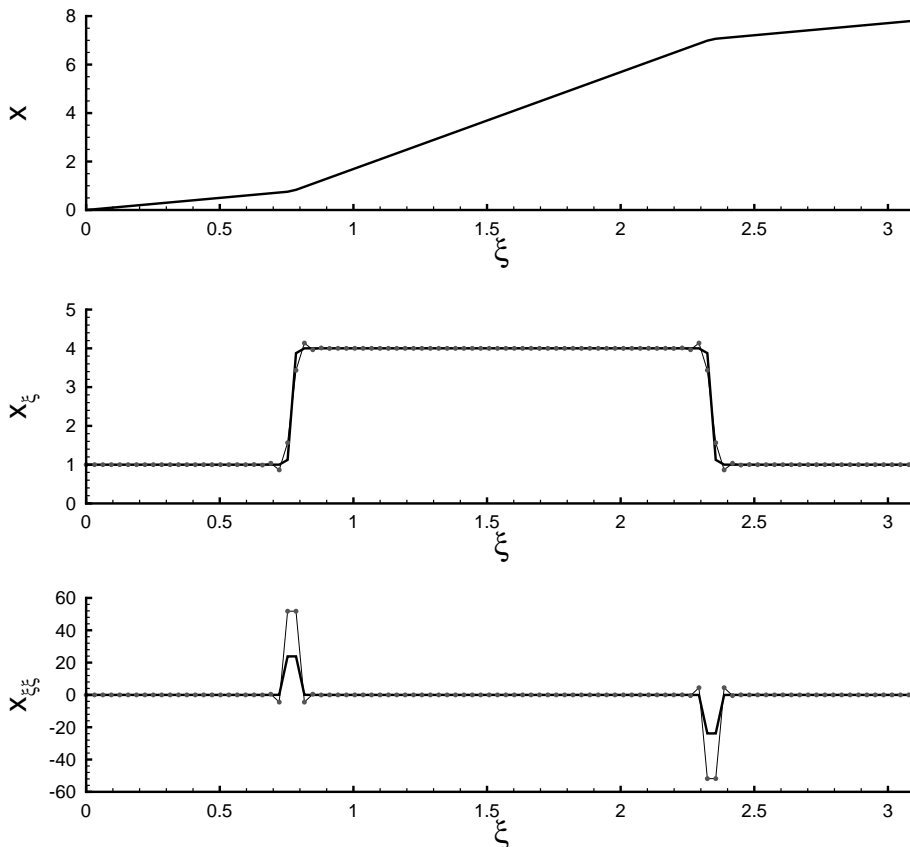


Figure 11: Grid transformation $x(\xi)$ with the corresponding metric coefficients x_{ξ} and $x_{\xi\xi}$. The black solid line corresponds to the analytical metric coefficients. The numerically computed metric terms are given by the thin grey line with the discrete grid points indicated by dots.

The time steps are $\Delta t = 0.015705$ and $\Delta t = 0.0001353$ for the advection and diffusion problem, respectively. In case of the pure advection, the wave of the initial condition is resolved with 125 time steps per period. With the high temporal resolution, effects due to the time-integration scheme can be neglected. For both cases, a total number of 500 time steps has been computed. The resulting computed time of the convection case corresponds to one flow-through time of the domain. For the diffusion problem, the amplitude is halved after the computed time steps. The exact solution is shown in figure 12 for both cases after the corresponding computed time.

3 One-dimensional Numerical Investigation

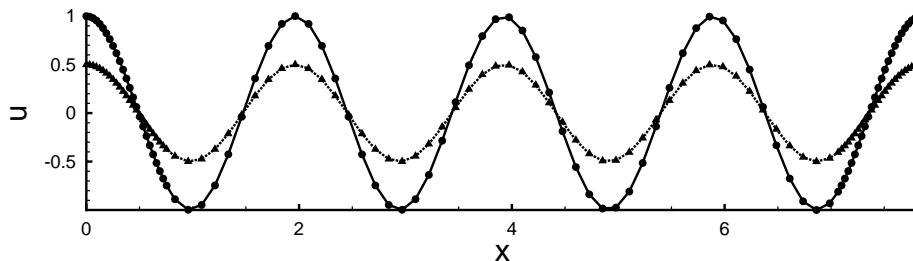


Figure 12: Exact solutions for the advection problem (solid line with circles) and the diffusion problem (dashed line with triangles). The time corresponds to one flow-through time and one half-life period, respectively. The symbols refer to the grid points.

3.2.1 Advection Case

For the advection case, the quality of the computed first derivative is time dependent. As the wave travels through the domain, the largest error occurs when the maximum of the first derivative is located near positions of coarsening or refinement of the grid. Figure 13 shows the temporal evolution of the solution for 2^{nd} -order explicit and 4^{th} -order compact FDs, both for analytical and numerical metric coefficients. During the temporal interval of 100 time steps, shown here, the wave travels along a distance of 1.57. The compact scheme provides an almost accurate solution with no observable differences between the two methods of grid transformation. The low-order methods show the same phase error increasing with time.

The difference between the two grid-transformation methods is the strong generation of wiggles for analytical metrics. They are firstly generated at the coarsening of the mesh ($x = 0.8$). Having a negative group velocity, the wiggles move upstream and enter the domain at the right due to the periodicity of the problem. Between time step 100 and 200, the region of refinement ($x = 7.0$) is reached. Further on, the wiggles move into the coarse region and increase furthermore, spoiling the solution.

For the compact 4^{th} -order stencils, figures 14 a) and b) show the different solutions in the region of grid stretching at time step 400 and 500, respectively. Time step 400 corresponds to $u \approx 0$ and thus the maximum of $|\partial u / \partial x|$ located at the beginning of grid stretching. At both time steps, the solution of the biased compact FDs and the numerical metric coefficients is similar. The computation using analytical metric coefficients shows the worst results resulting in wiggles in the area of fine grid spacing. For the computation using numerical metric coefficients, wiggles are also present but much smaller.

3 One-dimensional Numerical Investigation

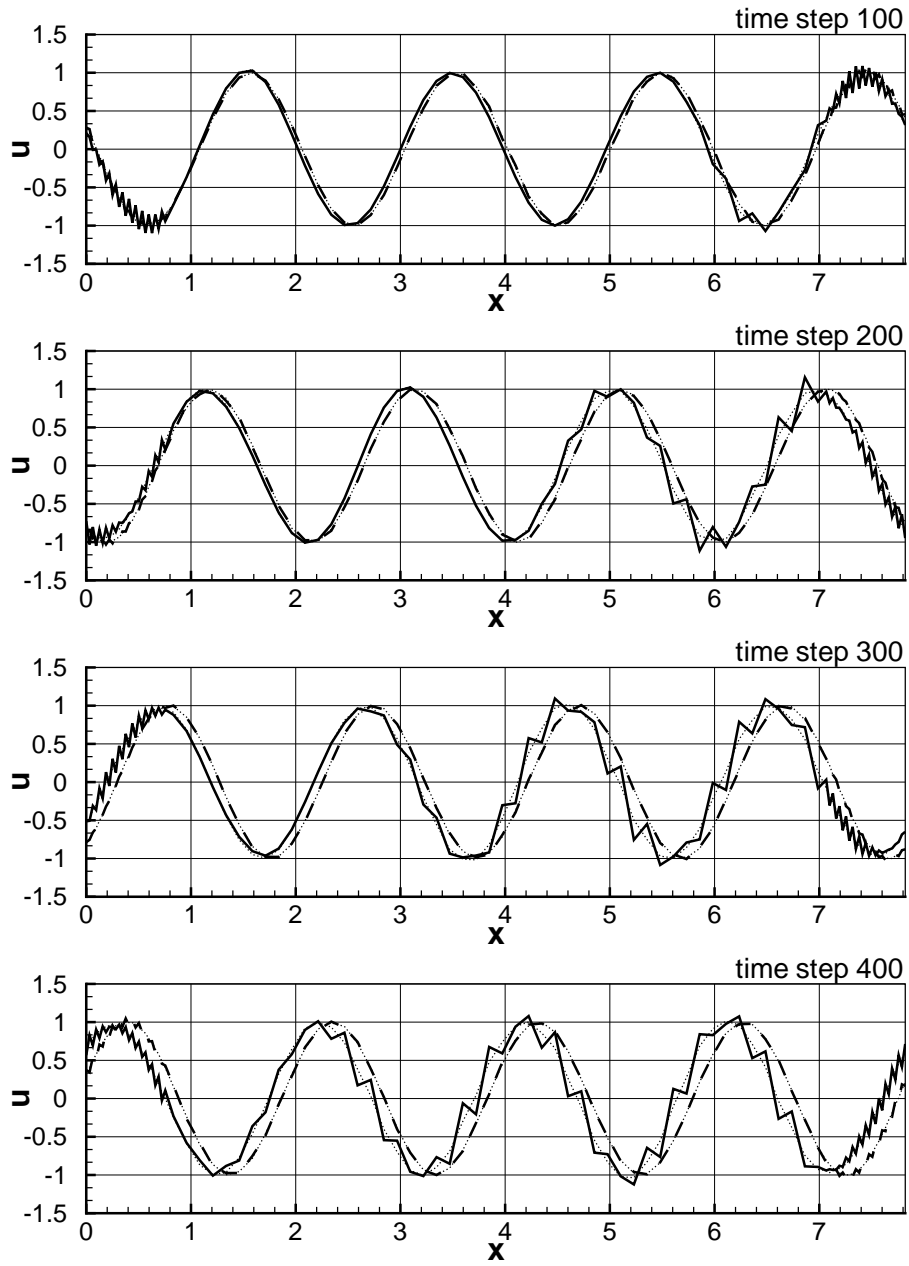


Figure 13: Solution of the advection problem at various time steps. The dotted line corresponds to numerical metric coefficients. The solid and dashed lines refer to analytical metric coefficients based on 2nd-order explicit and 4th-order compact FDs, respectively.

3 One-dimensional Numerical Investigation

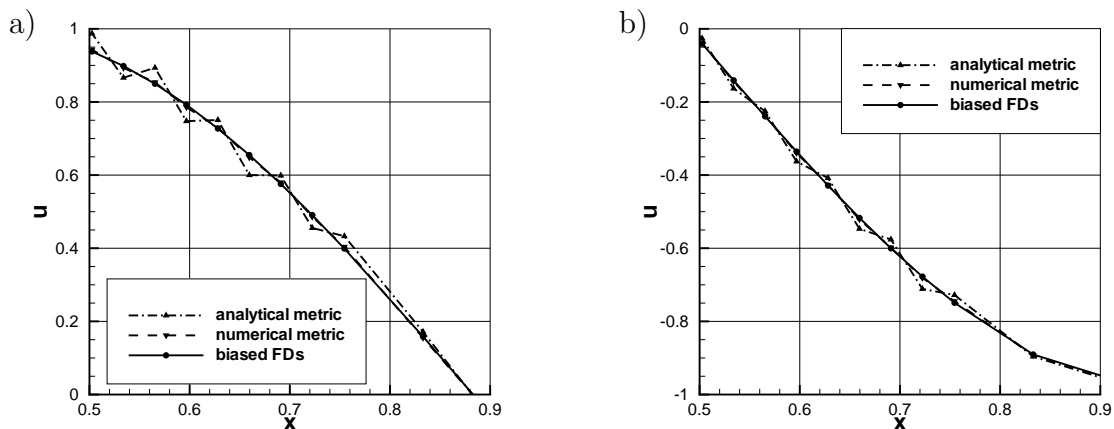


Figure 14: Solution of the advection case based on 4th-order compact FDs: a) time step 400 (80% of flow-through time), b) time step 500 (one flow-through time).

In order to evaluate the difference between explicit and compact stencils for this numerical example, equation (1) has been computed using the explicit five-point stencils as well. In figures 15 a) and b), the solution is shown for time steps 400 and 500, respectively. The difference between the biased finite difference, the analytical and the numerical grid transformation is similar to the computation based on the compact scheme. The explicit stencils give a larger wiggly mode which is most obvious at time step 400 for the analytical metric coefficients.

Having a periodic domain, a Fourier analysis in x -direction is applied to evaluate the dispersion properties of the three grid-stretching implementations. In figures 16 a) and b), the streamwise spectrum is shown. The exact solution is a single amplitude of $u = 1$ at a spanwise wavenumber $\alpha/\alpha_0 = 4$, indicated by the dotted line in the spectra. At timestep 400, the analytical metric coefficients give an amplitude of $4 \cdot 10^{-2}$, almost constant along the whole spectrum. After one whole flow-through time (time step 500), the high-wavenumber amplitudes decrease to $5 \cdot 10^{-3}$. For the lower wavenumbers, only a minor reduction occurs. The numerically computed metric coefficients lead to a spectrum approximately one magnitude smaller for both time steps considered here. The biased scheme provides a smooth decay for high wavenumbers. At low wavenumbers, the spectra of numerical metric coefficients and biased compact finite differences are almost identical.

3 One-dimensional Numerical Investigation

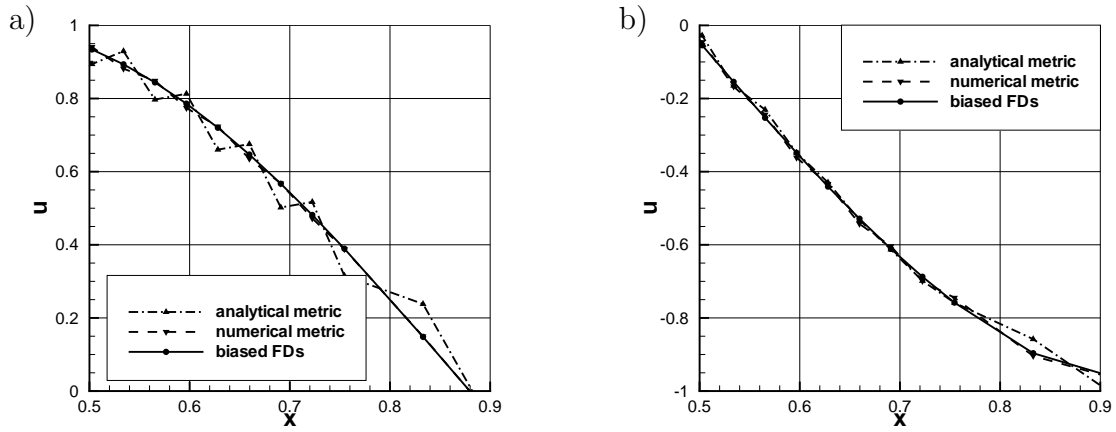


Figure 15: Result as figure 14 but for 4th-order explicit FDs: a) time step 400 (80% of flow-through time), b) time step 500 (one flow-through time).

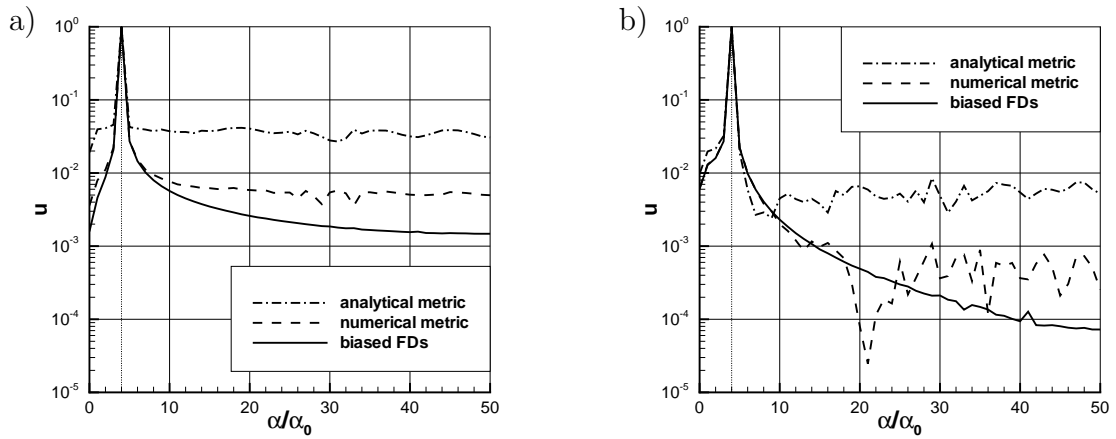


Figure 16: Streamwise spectrum for the advection case, based on 4th-order compact FDs: a) time step 400, b) time step 500.

3 One-dimensional Numerical Investigation

3.2.2 Diffusion Case

Without convection speed ($c = 0$), the time dependence of the accuracy of the second derivative is only due to its decreasing amplitude. Thus, it is sufficient to consider only one time step. Figure 17 a) compares the solutions for the compact scheme at time step 500, corresponding to one half-life period. Both numerical metric coefficients and biased FDs give a good approximation. For the analytical metric coefficients, the damping rate in the vicinity of the coarsening of the grid is too small. In the highly resolved part of the domain, shown in figure 17 b), the damping rate is slightly too large. If the explicit five-point stencils are used, no relevant difference to the compact schemes can be observed.

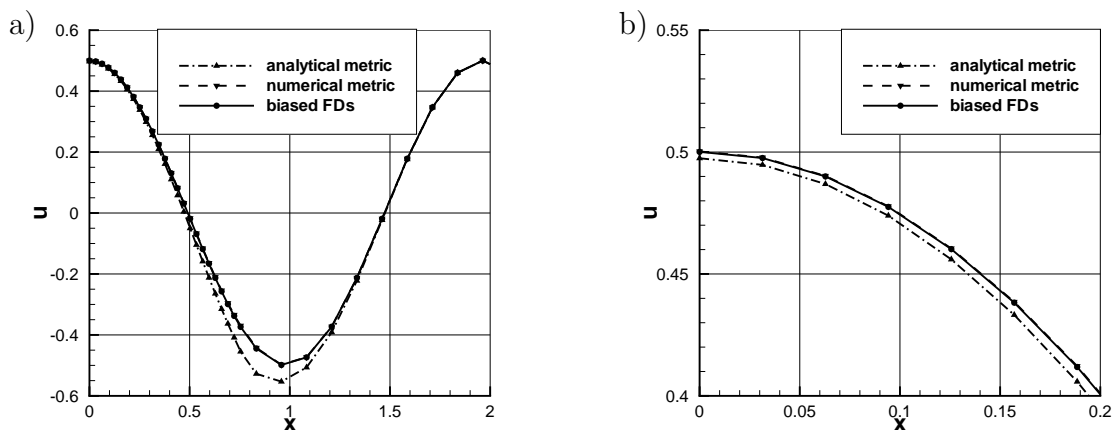


Figure 17: a) Comparison of the three grid-stretching mechanisms (4^{th} -order compact FDs) for the diffusive case at time step 500 (one half-life period), b) detailed view.

The instantaneous error $|u - u_{exact}|$ of the compact schemes is plotted in figure 18 a). The biased compact finite differences show the lowest error in the range of $4 \cdot 10^{-5}$ with the main derivation located in the stretched section of the grid. Both analytical and numerical metric coefficients have a maximum error of $8 \cdot 10^{-2}$ and $4 \cdot 10^{-3}$, respectively. The error peaks are at the locations of coarsening and refinement while in the coarse region, the error is similar to the one of the biased FDs. The streamwise spectrum of the diffusion case is given in figure 18 b) where the exact solution $u = 0.5$ at $\alpha/\alpha_0 = 4$ is indicated by a dotted line. The spectra of the biased FDs and the numerical metric coefficients show a smooth decay for the higher wavenumbers and the amplitudes of the lower wavenumbers decline to values of $3 \cdot 10^{-3}$. The numerically computed metric

4 Application to Boundary Layer Instability

coefficients show an additional oscillation for the higher wave numbers. For the analytical metric coefficients, this oscillation is larger by almost one order of magnitude and the low-wavenumber amplitudes decrease less.

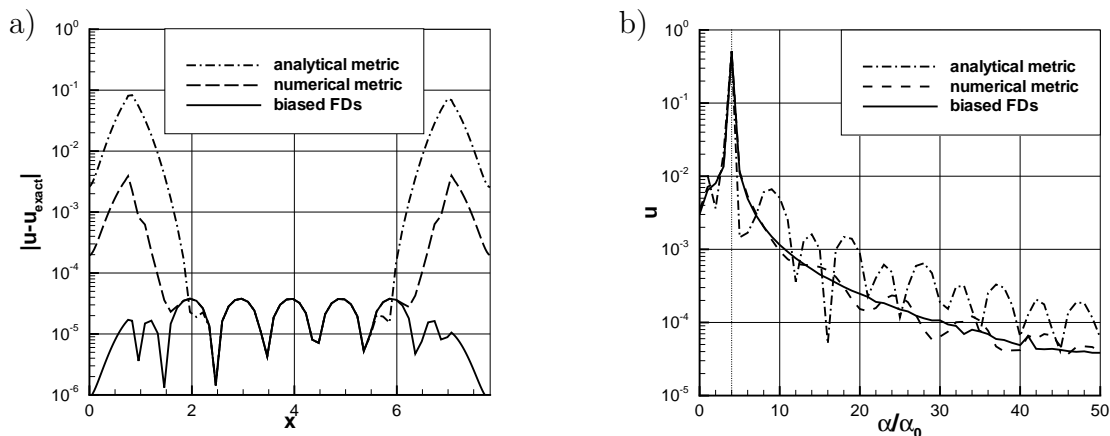


Figure 18: a) Error of the three different grid stretching mechanisms at half-life level for the diffusion case.
b) Streamwise spectrum for the diffusive case at time step 500.

4 Application to Boundary Layer Instability

4.1 DNS Code

To test different grid-stretching techniques in a real example, the DNS-code NS3D is applied here for a two-dimensional case. For a detailed description of the code the user is referred to [2, 4]. Computation is done in non-dimensional quantities: the velocities are normalized by the reference velocity \bar{U}_∞ and all other quantities by their inflow values, marked with the subscript ∞ . Length scales are made dimensionless with a reference length \bar{L} , specified by the Reynolds number $Re = \rho_\infty U_\infty L / \mu_\infty$, and the time t with \bar{L} / \bar{U}_∞ , where the overbar denotes dimensional values. Temperature dependence of viscosity μ is modelled using the Sutherland law and a constant Prandtl number is assumed.

The simulation is carried out in a rectangular domain with x and y being the stream-wise and normal direction, respectively. The spatial discretization is done by compact

4 Application to Boundary Layer Instability

finite differences of 6th order. To avoid aliasing, alternating up- and downwind-biased finite differences are used for convective terms [10]. Biased finite differences are not implemented in the code. Thus, only analytical and numerical metric coefficients are considered here. The first derivatives of viscous terms as well as the second derivatives are based on standard 6th-order compact finite differences. These stencils are also used for the computation of the numerical metric coefficients as dealiasing is of course not required for the geometry. The method of grid-adapted biased FDs is not implemented in the DNS code. For more general grid transformations like curvilinear grids with $x = x(\xi, \eta)$, $y = y(\xi, \eta)$, its realization is extremely awkward, especially for compact FDs. Additionally, dealiasing by alternating up- and downwind biased FDs would not be possible.

Time integration of the conservative variables is done using the standard 4th-order Runge-Kutta scheme as it is the case for the one-dimensional analysis. For the case presented here, the code is run in disturbance formulation. This means that the defined baseflow is considered to be a steady-state solution. At the inflow, all quantities are prescribed using the baseflow and additional time dependent disturbances. For the boundary at the bottom of the domain, an isothermal wall with no-slip condition and extrapolation of the pressure is used. At the freestream, a one-dimensional characteristic boundary condition according to Giles [8] is applied. To avoid reflections from the outflow boundary, a damping zone [9] along the last 40 grid points ramps the disturbances smoothly to zero.

4.2 Results

In order to compare different grid stretching mechanisms for an actual simulation of fluid mechanics, the streamwise evolution of a Tollmien-Schlichting wave in a subsonic boundary layer is computed. The boundary layer is obtained from a similarity solution with a Mach number $Ma = 0.8$ and a freestream temperature $T_\infty = 280K$. The wall temperature is fixed to $T_{wall} = 296K$. The Reynolds number $Re = \rho_\infty U_1 \delta_1 / \mu_\infty = 1000$ is based on the displacement thickness δ_1 at the inflow boundary, with $\delta_1(x_0) = 1$. Figure 19 shows the baseflow values at the inflow.

The streamwise coordinate has its origin at the leading edge of the flat plate and ranges from $x_0 = 337$ to $x_E = 895$ inside the domain. The normal coordinate runs from $y = 0$ at the wall up to $y = 22.35$ at the upper boundary. With the boundary layer thickness $\delta_{99}(x_0) = 2.95$ and $\delta_{99}(x_E) = 4.8$ at the inflow and outflow, respectively, the upper boundary condition does not affect the results. Two grids are used to investigate the influence of the different grid stretching mechanisms. The uniform grid resolves the streamwise direction with 330 points with $\Delta x = 1.6981582$, corresponding to 20 points

4 Application to Boundary Layer Instability

per wave length of the TS-wave. The fine solution on this mesh is intended to serve as a reference solution. The stretched grid uses the same Δx at the beginning and at the end of the domain. In between, the spacing is increased by a factor of four. Thus the TS-wave is resolved only with 5 points per wavelength in the coarse region of the mesh. With the same extent as for the equidistant reference case, now only 180 points are needed in x direction. For both grids, the normal direction is discretized with 150 points and an equidistant spacing $\Delta y = 0.15$. The damping zone is applied over the last 40 grid points from $x(\xi = 140) \approx 827$ onwards. Thus the stretched part of the grid is located roughly in the middle of the domain without damping zone.

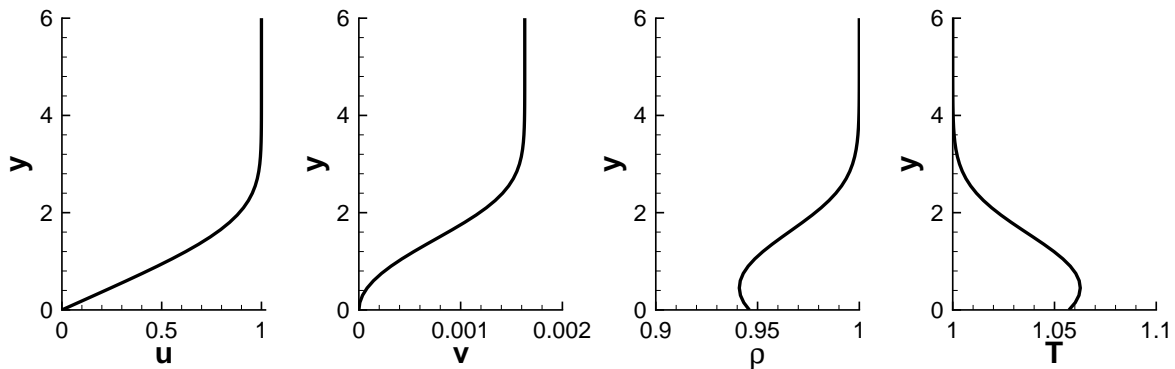


Figure 19: Baseflow condition at the inflow $x_0 = 337$.

Based on spatial linear stability theory (LST), a fundamental frequency of $\omega_0 = 0.0688$ has been chosen for disturbance generation, being the most amplified disturbance at the inflow. The flow is excited at the inflow with the eigenfunction of the Tollmien-Schlichting (TS) wave with the fundamental frequency ω_0 . In the DNS, the prescribed amplitudes for each quantity are scaled such that the maximum of \hat{u} is 0.005. The time step for all simulations is $\Delta t = 0.06088$, thus resolving one period of the TS wave with 1500 timesteps. In total 40 periods have been computed with the output of the last period being used for Fourier analysis. The simulated time corresponds to roughly 6.5 flow through times, based on the freestream velocity $U_\infty = 1$.

Figure 20 shows the streamwise development of the maximum amplitude along the wall-normal direction of u for the fundamental frequency ω_0 . For the uniformly fine grid, the amplitude reaches its maximum of $\hat{u} = 0.025$ at $x \approx 720$. For the stretched grid, wiggles are generated in the coarse region of the mesh. Compared to the solution on the

4 Application to Boundary Layer Instability

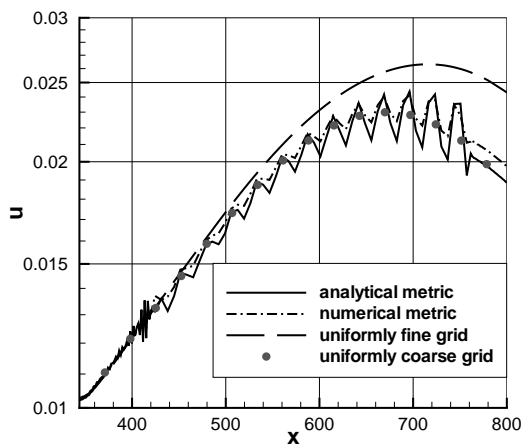


Figure 20: Amplitude development of the u-velocity component for the fundamental frequency $\omega_0 = 0.0688$.

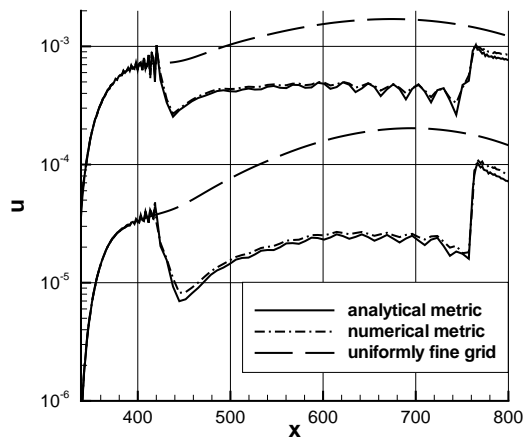


Figure 21: Amplitudes of the u-velocity component for the first two higher harmonics (black = $2 \cdot \omega_0$, grey = $3 \cdot \omega_0$).

uniformly fine grid, the amplitudes on the stretched grid are reduced by 10 to 20 %. For the analytical grid transformation, the wiggles in the coarse region are almost twice as strong compared to numerically computed metric coefficients. The reason for the reduction of the amplitude is investigated by comparing the amplitudes to a simulation on a uniformly coarse grid with $\Delta x = 4 \cdot \Delta x_0$. Since the constantly coarse resolution also affects the front part of the grid $x < 420$, the level of the amplitude differs. From the good agreement between linear stability theory and DNS results given below in figure 22, we find the growth to be clearly determined by linear mechanisms. Thus the amplitude obtained from the uniform coarse mesh can be shifted along the logarithmic ordinate to match the curves at $x = 420$, as done in figure 20. Apart from the wiggles due to the non-uniform grid, the mean amplitude corresponds well to the solution on the uniformly coarse grid. Thus the reduced amplitude is not due to the change in resolution but simply caused by the coarser mesh itself in the middle of the domain. In figure 21, one can see that the higher harmonics are damped in the region with coarse spacing. This is due to the numerical dissipation by the used alternating forward-backward biased differences required for dealiasing. This strategy is used in x - and y -direction with the FDs providing appropriate stabilization for nonlinear simulations including super- and hypersonic Mach numbers. In the case considered here, the number of points per wavelength are 5, 2.5

4 Application to Boundary Layer Instability

and 1.75 for the fundamental wave and its first two higher harmonics, respectively. Thus in the coarse region of the mesh, numerical damping counteracts physical amplification and nonlinear generation. After refinement of the grid the higherharmonics are increased again but do not reach the corresponding values of the reference solution.

The amplification rates of the TS wave for the three computed cases are compared with spatial linear stability theory in figure 22. For the uniformly fine grid, the amplification rate of the TS wave corresponds well to the result from LST which slightly underpredicts $-\alpha_i$ further downstream. The detailed view of the amplification rate in figure 23 reveals a saw-tooth modulation of the amplification rate, especially in the region of grid stretching ($x = 420$). In the region with coarse spacing, these oscillations are first reduced but then grow further downstream (figure 22). At the position of refinement ($x = 760$) maximum variations of 0.035 and 0.017 can be observed for the analytically and numerically computed metric coefficients, respectively. With the following fine stepsize, only a slightly increased value of α_i can be observed, compared to the reference solution. Especially for the sensitive quantity α_i , it can be seen that wiggles spread upstream ($x < 420$) due to the negative group velocity invoked by the decreasing k_{mod}^* .

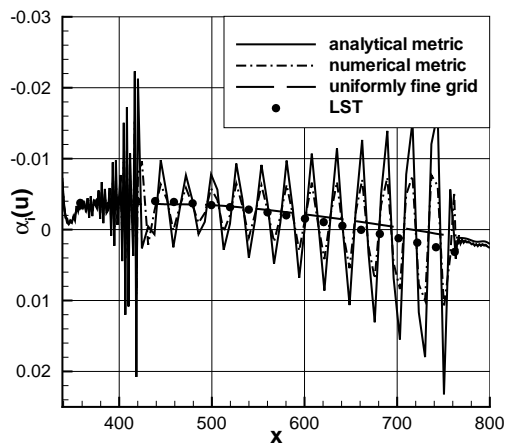


Figure 22: Amplification rate $-\alpha_i$ of the TS-wave, based on the wall-normal maximum.

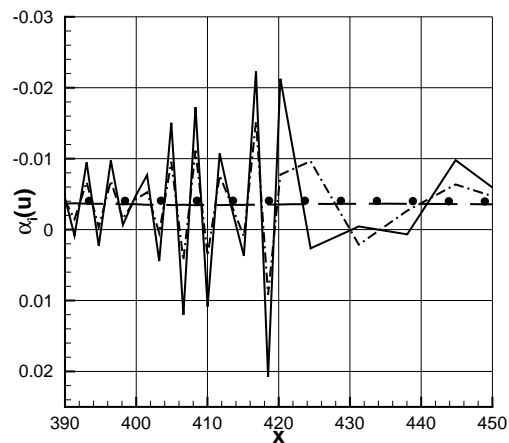


Figure 23: Detailed view of the amplification rate the region of grid stretching (symbols and lines as in left figure).

5 Conclusions

According to the one-dimensional advection-diffusion example, the alternating resolution generates broadband disturbances which are larger in case of analytical metric coefficients. From the position of refinement the saw-tooth mode travels upstream where it is slightly damped by viscosity and dissipation of the numerical scheme. With the wiggle mode on the coarse mesh having a group velocity in the direction of coarsening, the same wave travels from $x = 420$ in positive x -direction. The smaller oscillations travelling in streamwise direction are probably due to the lower amplitude compared to the position of refinement. Both oscillations may cancel to some extent ($430 < x < 440$ in figure 23). As shown by figure 3, the group velocity of the saw-tooth mode on the fine parts of the grid does not have to point in the same direction as its coarse-mesh counterpart. Hence we can also see upstream propagating oscillations for $x < 420$. Since these are not visible at the refinement of the grid where the amplitude of the TS-wave is larger, they are more likely generated by the upstream travelling saw-tooth mode than by the physical instability waves.

5 Conclusions

The effects of non-uniform grids on the accuracy of the discretization are investigated theoretically and numerically for a linear advection-diffusion problem as well as for the streamwise development of a Tollmien-Schlichting wave in a flat-plate boundary layer. The following three methods are considered: biased finite differences with the coordinates of the non-uniform mesh included directly in the stencil, grid transformation based on analytical metric coefficients or numerically computed metric terms. Considering a continuously stretched grid as well as an almost instantaneous alteration of the resolution covers the most of the variety of stretched grids. We point out that the strong mesh variations used here are used to illustrate the effects of non-uniform grids.

Despite one might think analytically prescribed metric coefficients are the best choice, the theoretical analysis shows that this method is of zeroth order on the physical grid or may even cause inconsistent results. Furthermore it yields wrong phase and group velocities even for arbitrarily resolved problems. In case of numerical metric terms, discretization errors of the derivatives in computational space and of the metric coefficients seem to cancel each other. The scheme is now of second and zeroth order on the non-uniform grid for first and second derivatives, respectively. It is notable that the order can not be increased but the magnitude of the error is decreased by a larger stencil. Biased finite differences show always the same order as on equidistant grids.

The theoretical analysis is not possible for compact finite differences since the complete grid is included by the left-hand side. Therefore a one-dimensional advection-diffusion

5 Conclusions

problem is investigated numerically. For all three methods, a rapidly changing resolution creates a broad spectrum of artificial disturbances. Numerical metric coefficients show almost the same behavior as biased finite differences. Using analytical metrics gives the worst results with their error being one order of magnitude larger than the one for the numerically computed metric coefficients. The use of compact finite differences reduces the absolute error by almost one order of magnitude for the advection case.

Finally the discretization based on analytical and numerical grid transformation is applied to the spatial evolution of a Tollmien-Schlichting wave in a compressible boundary layer. The coarsening results in a smaller growth rate of the Tollmien-Schlichting wave which is not caused by the variation of the mesh itself but only by the worse resolution. The latter causes a saw-tooth like behaviour of the amplification rate which can be explained by the theoretical analysis and the one-dimensional numerical example. Accordingly, numerical metric coefficients yield better results than analytical ones.

With the results obtained here, the approach of Zhong and Tatieni [17] is acknowledged since they use the favorable properties of the biased finite differences for pure grid stretching and grid transformation only for the deformation of the mesh.

Implementation and computational costs are a relevant issue for a numerical method as well. On non-moving grids, metric terms or coefficients of the biased finite differences are computed only once at the beginning of the simulation. Compared to the number of time steps for real applications, this part of the initialization is not a relevant computational effort for all methods. Though, additional multiplications occur for both grid transformation methods. In what way this may affect the computational costs strongly depends on the solved equations. It might be observable for incompressible flows; in case of the compressible Navier-Stokes equations, where all terms are non-linear, no additional computational costs could be observed. On the other hand, grid transformation has two advantages: i) it is by far more efficient to implement a compact discretization on a deformed mesh with $x = x(\xi, \eta)$ and $y = y(\xi, \eta)$, for fully three-dimensional grids this has to be considered even more severely, and ii) simple de-aliasing can be implemented easily by using alternating up- and downwind-biased finite differences as on a uniform mesh without additional computational costs.

References

- [1] N. Adams. Direct simulation of the turbulent boundary layer along a compression ramp at $M=3$ and $Re_\theta=1685$. *J. Fluid Mech.*, 420:47–83, 2000.
- [2] A. Babucke. *Direct Numerical Simulation of Noise-Generation Mechanisms in the Mixing Layer of a Jet*. PhD thesis, Universität Stuttgart, 2009.
- [3] A. Babucke, M. J. Kloker, and U. Rist. DNS of a plane mixing layer for the investigation of sound generation mechanisms. *Computers and Fluids*, 37(4):360–368, 2008.
- [4] A. Babucke, J. Linn, M. Kloker, and U. Rist. Direct numerical simulation of shear flow phenomena on parallel vector computers. In *High performance computing on vector systems: Proceedings of the High Performance Computing Center Stuttgart 2005*, pages 229–247. Springer Verlag Berlin, 2006.
- [5] T. Colonius, S. K. Lele, and P. Moin. Boundary conditions for direct computation of aerodynamic sound generation. *AIAA Journal*, 31(9):1574–1582, Sept. 1993.
- [6] T. Colonius, S. K. Lele, and P. Moin. Sound generation in a mixing layer. *J. Fluid Mech.*, 330:375–409, 1997.
- [7] H. Fasel. Investigation of the stability of boundary layers by a finite-difference model of the Navier-Stokes equations. *J. Fluid Mech.*, 78:355–383, 1976.
- [8] M. B. Giles. Nonreflecting boundary conditions for Euler equation calculations. *AIAA J.*, 28(12):2050–2058, 1990.
- [9] M. Kloker and U. Konzelmann. Outflow boundary conditions for spatial Navier-Stokes simulations of transitional boundary layers. *AIAA J.*, 31(4):620–628, 1993.
- [10] M. J. Kloker. A robust high-resolution split-type compact FD scheme for spatial DNS of boundary-layer transition. *Appl. Sci. Res.*, 59:353–377, 1998.
- [11] S. K. Lele. Compact finite differences with spectral-like resolution. *J. Comput. Phys*, 103:16–42, 1992.
- [12] A. Pagella, A. Babucke, and U. Rist. Two-dimensional numerical investigations of small-amplitude disturbances in a boundary layer at $Ma=4.8$: Compression corner versus impinging shock wave. *Physics of Fluids*, 16(7):2272–2281, 07 2004.

References

- [13] R. D. Sandberg, L. E. Jones, N. D. Sandham, and P. F. Joseph. Direct numerical simulation of noise generated by airfoil trailing edges. In *13th AIAA/CEAS Aeroacoustics Conference (28th AIAA Aeroacoustics Conference)*. AIAA 2007-3469, 2007.
- [14] R. K. Shukla and X. Zhong. Derivation of high-order compact finite difference schemes for non-uniform grid using polynomial interpolation. *J. Comput. Phys.*, 204:404–429, 2005.
- [15] M. R. Visbal and D. V. Gaitonde. On the use of higher-order finite-difference schemes on curvilinear and deforming meshes. *J. of Comp. Physics*, 181(1):155–185, September 2002.
- [16] D. You, R. Mittal, M. Weng, and P. Moin. Analysis of stability and accuracy of finite-difference schemes on a skewed mesh. *J. Comput. Phys.*, 213:184–204, 2006.
- [17] X. Zhong and M. Tatineni. High-order non-uniform grid schemes for numerical simulation of hypersonic boundary-layer stability and transition. *J. Comput. Phys.*, 190:419–458, 2003.